A three dimensional numerical quantum mechanical model of field electron emission from metallic surfaces covered with carbon adsorbates

Maykel Márquez-Mijares, Bruno Lepetit

A three dimensional numerical quantum mechanical model of field electron emission from metallic surfaces covered with carbon adsorbates.

Maykel Márquez-Mijares*

Instituto Superior de Tecnologías y Ciencias Aplicadas. Havana University.
Ave. Salvador Allende No. 1100. Quinta de Los Molinos, Plaza, La Habana 10600, Cuba.
Université de Toulouse; UPS; Laboratoire Collisions Agrégats Réactivité,
IRSAMC; F-31062 Toulouse, France and
CNRS; UMR 5589; F-31062 Toulouse, France

Bruno Lepetit†

Laboratoire Collisions Agrégats Réactivité,
UMR5589, Université de Toulouse, CNRS,
Bât. 3R1b4 - 118 route de Narbonne 31062 Toulouse Cedex 09, France

(Dated: July 3, 2019)

Abstract

The effect of metallic surface contamination on field electron emission is investigated for the first time using a three dimensional quantum mechanical model. The plane wave periodic version of the density functional theory is used to obtain wavefunctions and potentials. Local and averaged emitted current densities are obtained from them using time dependent perturbation theory. This method is used to study the effect of the presence of carbon adsorbates on emission from tungsten surfaces. Fowler-Nordheim plots which provide the dependence of the emitted current with the external electric field show that carbon contamination inhibits emission. Significant differences with the results of the analytical Fowler-Nordheim model are observed. Emissions images (i. e. the spatial dependence of the emitted current density) are presented to identify the important emission spots. These images are significantly different from the electronic density plots usually presented to model constant height scanning tunnelling microscope images. Analysis of the emitted current density energy distributions in the light of the projected local density of states provides a deeper understanding of the emission process.

I. INTRODUCTION

There has been recently a renewed interest in the nuclear fusion industry community[1,2] on the problem of field electron emission from metals resulting from the application of external static electric fields[3,4]. Indeed, such emission can cause electrical breakdowns in vacuum systems and thus limit performances of fusion plasma heating devices[1,5–7]. This emitted current can be reduced by raising the pressure in the vacuum system from ultrahigh vacuum to pressures of the order of $10^{-4} - 10^{-2}$ Pa[8–14]. This gas effect has been investigated recently in details for tungsten carbide and tungsten cathodes in a combined experimental and theoretical effort[15–17]. A reversible mechanism has been proposed. It involves the formation of nanoscale carbon based emitting structures by polymerization of hydrocarbon contamination with low-flux ion bombardment at low pressure and the destruction of these structures by high flux ion bombardment at sufficiently high pressure. This proposal is consistent with the correlation observed experimentally between field emission intensity and surface carbon concentration[17].

The original Fowler-Nordheim model (FN)[3] describes field emission as an electronic quantum mechanical tunneling process through a crude triangular potential barrier. This simple model was readily improved by Nordheim[18], who added the charge-image interaction to the triangular one. There was however a mistake in the improved emission model which was noted only in 1953[19]. Soon later, Murphy and Good (MG) included correctly the same charge-image interaction in an extended model which encompasses both thermoionic and field emissions. The model was also extended to include curved emitters[20] and a more realistic description of the local density of states at the surface[21]. Formally simpler and more universal formulations of these models have later been proposed[22,23]. Although they have been widely and successfully used over the years, all these models rely on a crude one dimensional, semi-empirical description of the emitting electrode. More quantitative non empirical models have been designed in recent years, in particular in the context of the development of carbon based nanomaterials (for reviews, see ref. 24,25). Most of them rely on Density Functional Theory (DFT). One class of such models adapts the Fowler-Nordheim picture to the context of DFT potentials[25–27]. A second class uses Schrödinger-like equations, either time dependent or time independent, to describe the emitted electron dynamics. Among time independent methods are wavefunction propagation methods[28–34].

Alternatively, non-equilibrium time independent Green 's function[35] and Fisher-Lee 's transmission formulation[36] have also been used. Time dependent methods involve wavepacket propagations to describe electron emission[37–39]. However, these methods have found limited applications because the applied external field is relatively weak when compared to the intrinsic electrostatic field in the emitter at the atomic scale. This suggests that perturbative methods, as the one implemented here, are better adapted to model field emission. We proposed recently[40,41] a method to compute emitted currents based on plane wave DFT and electronic wavepacket time propagation within the perturbation theory framework. This method was tested on the emission from flat[40] and corrugated[41,42] clean tungsten.

The present paper is a continuation of the effort to understand the influence of the ambient gaz pressure on emission using this first principles based method. Up to now, the impact on emission of carbon contamination was estimated roughly with FN type models and DFT evaluations of the work function for surfaces with or without carbon[17,43]. In the present paper, we go one step further by performing accurate computations of the emitted currents for different carbon adsorbate configurations. This effort represents, to our knowledge, the first application of quantitative DFT type models to contaminated emitters. It is a step toward more realistic computer models of field emission. We describe in section II the computational method which we have implemented. We present in sub-section II A the formalism and in sub-section II B details about our implementation. In section III, we show the emitted current densities resulting from this model for a tungsten surface, either clean (0ML) or covered with one (1ML) or two (2ML) monolayers of carbon. We compare these results with the ones of FN (triangular barrier without charge-image interaction) and MG (including charge-image interaction but at zero-temperature) models. The obtained current densities are interpreted with the help of emission images and emission energy spectra calculations.

II. COMPUTATIONAL METHOD

A. General framework

As our computational method has already been described in previous papers[40,41], we provide here only sketchy information. We consider the electrons of a metallic slab covered

or not with carbon at 0 K temperature, infinite in the x and y directions, and subjected to an external field $\mathbf{F}$ parallel to z which induces an electronic current flowing from the metal into the vacuum. We assume that this current is weak enough so that first order perturbation theory can be used to model accurately this process and we use its time dependent version.

The electrons occupy the orbitals $\Psi_m(\mathbf{r}, \mathbf{F} = 0)$ defined by:

$$(T + U(\mathbf{r}, \mathbf{F} = \mathbf{0}))\, \Psi_m(\mathbf{r}, \mathbf{F} = 0) = \epsilon_m\, \Psi_m(\mathbf{r}, \mathbf{F} = 0) \tag{1}$$

T is the electronic kinetic energy operator and $U(\mathbf{r}, \mathbf{F} = \mathbf{0})$ is the total potential energy in the absence of external field experienced by an electron of the material located at $\mathbf{r}$, m the corresponding set of quantum numbers. Periodic conditions are applied at the boundary of a volume Ω consisting of N_k unit cells, where N_k is the number of k-points used to sample the first Brillouin zone. The orbitals are normalized such that they correspond to one electron charge over Ω. The effect of the external field is described by time dependent perturbation theory which provides a "state current" I_m, the leakage rate of each orbital $\Psi_m(\mathbf{r}, \mathbf{F} = 0)$ into the vacuum. The total current emitted by Ω is: $I = 2\sum_m I_m$ (the factor 2 is due to spin degeneracy), from which averaged total and state current densities can be defined:

$$\bar{J} = \frac{I}{N_k A_{uc}} \quad \bar{J}_m = \frac{I_m}{N_k A_{uc}} \tag{2}$$

where A_{uc} is the emitting area of the unit cell. Our formalism[41] also provides state local current densities $J_m(x, y)$ which once summed yield the total local current density $J(x, y)$.

B. Numerical implementation

All DFT calculations were performed with the VASP (Vienna Ab initio Simulation Program) program developed at the Institut für Materialphysik of the Universität[44–47]. The electron-ion interaction for all atomic species (W and C) was described by the projector augmented wave potential (PAW)[48,49]. The valence electron configurations are built from $6s$ and $5d$ orbitals for tungsten (6 valence electrons) and from the $2s$ and $2p$ orbitals for carbon (4 electrons). The exchange-correlation energy has been calculated within the generalized gradient approximation (GGA) using the revised form (2002 version) of the Perdew, Burke, and Ernzerhof functional (PBE)[50,51]. Fractional occupancies were calculated using a second-order Methfessel-Paxton smearing function[52] with a width of 0.2 eV. The energy cutoff of the plane wave basis was chosen to be 460 eV.

For bulk tungsten, we consider a body-centered cubic (bcc) with a unit cell of two atoms. The optimized lattice parameter a was obtained with a reciprocal space of k-points generated automatically with the Monkhorst-Pack method[53] using a grid of $(16\times16\times16)$ points. These parameters ensured convergence of the total energies with an accuracy of the order of 5 meV. The tungsten (001) surface was modeled using a symmetric slab including 7 ions (fig. 1), the supercell length in the z direction was assumed to be as large as $20\,a$ to limit interactions induced by periodicity between adjacent slabs. The slab structure was optimized using also the Monkhorst-Pack scheme with $16\times16\times1$ points, the central layer only being fixed. The 1ML structure was obtained by optimizing the structure where all hollow sites are occupied by a single carbon atom (fig. 1). Optimization of the structure with 2 carbon atoms in the vicinity of the hollow site (2ML) induces a shift of the 2 carbon atoms in opposite directions of the diagonal of the unit cell side (fig. 1).

A larger supercell is used for the wavepacket propagation to avoid spurious reflection at its boundaries since we do not use absorbing potentials. Besides, a small step size has to be used to accommodate for the large kinetic of the escaping electrons accelerated by the external electric field. Convergence was achieved by using 1436 grid points in the [14.35 Å, 150 Å] interval for the z direction and 36 points in the [0 Å, 3.17 Å] interval for both x and y directions. The total current is obtained in our formalism by summation over state currents in an energy band including the Fermi level (the zero energy). At sufficiently low energy, electrons cannot escape because they are trapped by the confining electrostatic potential. We checked that convergence was achieved by keeping states belonging to the band [-5.5 eV, 0.2 eV]. Taking into account symmetries of the Brillouin zone, this amounts to 701, 728 and 5310 states for W(001), $C_H^{1ML}@W(001)$ and $C_H^{2ML}@W(001)$ configurations, respectively. For each state, the wavepacket was propagated during 600 step with a small time step of 4.8 as, which corresponds to a total propagation time of 2.88 fs.

III. RESULTS

A. Structures and Fowler-Nordheim plots

Fig. 1 shows the 3 structures considered in the present study. The pure tungsten (0ML) structure is optimized for the lattice parameter: $a = 3.172$Å, the corresponding cohesive

energy is −8.48 eV. Forming the (001) surface induces changes in the interlayer spacing as shown on table I. It breaks bonds between W atoms and frees electrons which become available to strengthen and shorten ($\Delta_{1\,2} < 0$) the bonds between the adjacent topmost layers. The present results differ by less than 1% from those of ref. 43 which were obtained with a larger cutoff energy (580 eV) and a larger tungsten basis set (14 valence electrons). This confirms the convergence of the present results.

The 1ML structure where each hollow (H) site is occupied with one carbon atom is the most stable mono layer structure. Indeed, the adsorption energy (8.8 eV) (table I) is larger for H sites than for bridge (6.52 eV) or top (4.65 eV) ones[43]. The presence of the carbon adsorbates increases the interlayer spacing (table I) between the topmost W layers. Indeed, carbon has a higher electronegativity than tungsten and depletes surface tungsten atoms from their electrons. As a result, the bond between the 2 tungsten layers closest to the surface weakens and $\Delta_{1\,2} > 0$. The 2ML structure considered here where both atoms are shifted from the H position in opposite directions is also the most stable one (H'+H' configuration of ref. 43). The weakening of the bond between the topmost W layers by the addition of one C atom is enhanced with the addition of a second, so that $\Delta_{1\,2}$ is further increased in the 2ML case (table I).

As the H sites are only 0.37Å (table I) above the metallic surface, the component perpendicular to the surface of the electrical dipole between adsorbate and metal is small for the 1ML configuration. Consequently, the work function is increased weakly from 4.12 eV for 0ML to 4.23 eV for 1ML (table I). On the contrary, adsorption of the second C atom far from the surface (1.42 Å, table I) in the 2ML case induces a strong perpendicular dipole and a large increase of the work function from 4.23 eV for 1ML to 6.24 eV for 2ML (table I). The length of the supercell used in our calculation is a in the x and y directions, reconstruction of the surface is thus forbidden in the 0ML and 1ML cases for which a minimum $\sqrt{2}\,a \times \sqrt{2}\,a$ supercell would be necessary for this process to be possible[43]. This approximation is expected to have limited impact on our results, but speeds up calculations significantly. In ref. 40, an even simpler model without relaxation at all was used, assuming a=3.179 Å. This model provided a work function of 4.2 eV for 0ML, which is also close to the present results (table I). Notice that the present value of the work function is consistent with most other computation results but differs significantly from experimental ones (see table 3 in ref. 43). This reflects the difficulty for theoreticians to meet an expected accuracy less than

0.1 eV, but presumably also for experimentalists to obtain conditions, in particular surface cleanliness, compatible with such a high accuracy.

Fig. 2 presents the final result of our DFT study. It is a Fowler-Nordheim plot for the averaged total emitted current densities in the 0ML, 1ML and 2ML configurations. Also shown are the results of the Fowler-Nordheim and Murphy-Good models using our computed work functions. Carbon contamination decreases emission, as expected from the increase of the work function in presence of carbon. All results show a decrease of $\bar{J}/F^2$ as a function of $1/F$ typical of field emission. The slopes in the Fowler-Nordheim plots associated to the DFT model are close to those associated to the FN and MG ones. This suggests that in all models the work function is the key driver which fixes the value of the slope, as expected. Tungsten covered with carbon and another pure material which would have the same work function would presumably give similar slopes in their DFT FN plots. The saturation observed at large field is not due to space charge limitation (like for instance in ref. 54,55). Saturation is reached in transmission through the Schottky barrier when it can be overcome classically. In the simple one dimensional MG model, saturation occurs at the sharp transition between flat and decreasing portions of the FN plots. Taking quantum effets fully into account changes this sharp transition into a smooth one (see for instance fig. 3 in ref. 40). Taking into account the three dimensions of the system blurs the transition even more, as it now occurs for different field values according to the location considered on the surface, since the interaction potential is now also location dependent. In all cases, the DFT results are in between the FN ones, which are the smallest, and the MG ones, which are the largest.

Our results extend up to the extremely high fields (50 V/nm). Experimental results on emission are available for fields larger than 10 V/nm, although most studies were performed below this limit. Recent reviews on these experimental studies are provided by refs. 56,57. It is therefore conceivable that the physical phenomena described in the present paper may be observable experimentally. Besides, using different materials with lower work functions, they may become observable at lower fields. Please also notice that the changes in slopes which appear on the low field part of the Fowler-Nordheim plots of fig. 2 may result from numerical noise in our computational model which becomes significant for the low current densities achieved in this field range. Energy transfers between sufficiently high field and material induce thermal effects at the electrode which can ultimately lead to its evaporation.

Describing this complex set of phenomena can be attempted at the atomic level with time dependent molecular dynamics type simulations (see for instance ref. 58) coupled to thermal and electrostatic solvers. A field emission model relating current to field at each time step for fixed nuclei remains a necessary ingredient of such molecular dynamics simulations[59]. The present work can be considered as an attempt to improve the accuracy of this ingredient of the full model.

B. Potentials and emission images

We now present intermediate data in order to understand better these final results. We know that emission is not uniform over the surface, even in the absence of adsorbate, and we first focus on the dependence of the emitted current density as a function of the position x, y on the surface. We anticipate that it can be influenced by two factors. One is the electrostatic potential profile along z for given x, y coordinates. The existence of barriers on this profile is expected to disfavor emission locally. The other factor is electronic density, emission originating from large density regions is expected to be favored. The relative importance of both factors can be assessed by inspection of fig. 3 which provides 2D plots of the electrostatic potentials and electronic densities. In the absence of external field, the electrostatic potential corresponds to the local work function (LWF) as defined in ref. 60–62 if the zero energy is chosen to be the one of the Fermi level. Far away from the surface, in the absence of external field, the local work function becomes constant and equals the usual work function. For the 0ML case, $F = 0$ V/nm (top left frame of fig. 3), the LWF increases steadily with z up to the work function value, 4.12 eV, along the line $x = y = 0.5$ (fractional coordinates) above the topmost W atom (layer # 7). However, at $x = y = 0$ (above the W atom belonging to layer # 6) it presents a maximum near $z = 20\,\text{Å}$ which reaches nearly 4.7 eV. From this point of view, one may expect emitted current density to be larger near $x = y = 0.5$ than near $x = y = 0$. When $F = 30$ V/nm (top right frame), there is indeed a saddle point near $x = y = 0.5$, $z = 21.5\,\text{Å}$ in the vicinity of which emitted electrons may escape predominantly from the surface. In the 0ML case, the electron density factor which is maximum near the central atom $x = y = 0.5$ also favors this emission path. These observations are consistent with the 0ML emission images shown on fig. 4 (top). For all fields considered, emission is indeed dominant in the vicinity of the central atom. Notice

however that the local current density varies with location by less than 10% so that the current is not so far from being emitted uniformly, as expected for a clean surface.

In the 1ML case, the contour lines are shifted to higher z above the C atom: for instance, the Fermi level at $x = y = 0$ moves from $z \approx 19\,\text{Å}$ in the 0ML case to $z \approx 20.5\,\text{Å}$ in the 1ML one. The potential barrier near $x = y = 0$ and $z \approx 20\,\text{Å}$ for 0ML is also shifted to higher z with little deformation for 1ML, its value is 4.79 eV. The saddle point near $x = y = 0.5$ and $z \approx 21.5\,\text{Å}$ for 0ML is still present for 1ML with little change. Therefore, the electrostatic potential factor still favors in the 1ML case emission from $x = y = 0.5$, which corresponds to a top site without C atom. On the other hand, the electronic density factor favors emission from the C atom at $x = y = 0$. It is indeed apparent that electronic density is highest near this location, this is a consequence of the large electronegativity of C. Both potential and density factors thus have opposite influences, and the net result of the competition is shown on fig. 4, central row. There is a gradual shift from predominant emission near W ($x = y = 0.5$) at low field to predominant emission near C ($x = y = 0.$) at large fields. The potential factor is the strongest at low field and the density one is the strongest at large field. This should be related to the efficiency of tunelling with respect to emission. A large contrast in emission between $x = y = 0$ where the barrier is present and $x = y = 0.5$ is expected when the barrier is large, and it is also expected to disappear when the barrier becomes thinner and even disappears at large field. In this latter case, the contrast in emission is controlled by the changes in electronic density with location: emission is then larger near C atoms. This dependence of the emitted density with location remains limited and is of the order of 10 %.

We investigate further with fig. 5 the correlation between LWF and local current emission in the 1ML case. The FN curves associated to the local current densities at W ($x = y = 0.5$) and C ($x = y = 0$) locations cross for an external field close to 27 V/nm and the emission near C is dominant at large field, as discussed. The slopes of these local current density curves are compared on fig. 5 with those resulting from the Fowler-Nordheim model, using the LWF for C and W locations, 4.79 eV (the maximum for $x = y = 0$) and 4.23 eV (the large z value for $x = y = 0.5$) respectively. The agreement between DFT based and Fowler-Nordheim based slopes is excellent. This indicates that the potential barrier which determines the LWF value controls emission locally.

Finally, in the 2ML case (fig. 3, bottom row), electronic potential and electronic density

factors both favor emission from the C atoms. Indeed, the potential barrier for emission is thinner near this location, as can be seen from the thickness of the potential band limited by the two 0 contour lines (Fermi level) on fig. 3, bottom right. Also, electronic density is larger in the vicinity of the C atom. Therefore, it is expected that emission is predominant from the vicinity C atoms for all field values, and this is what is observed on fig. 4, bottom row. Notice also that the contrast is sharper in the 2ML case than in the previous ones: emission from the vicinity of C atoms can be nearly two times larger than the one from the W surface atoms.

It is usual to perform numerical simulations of Scanning Tunneling Microscope (STM) images in constant height mode by plotting the electronic density at fixed distances from the surface. The densities for three distances $z = 18$, 19, 20 Å are illustrated on fig. 6. They are the same 3 dimensional electronic densities as the ones of fig. 3, but represented on different cut planes. It appears on these images that the density maxima reflect the positions of the atoms in their neighborhood. For instance, for 0ML and $z = 18$ Å, the maxima near the corners result from the proximity of W atoms, and the significant densities along the diagonals are traces of the formation of electronic bonds between W atoms located on adjacent layers. For 0ML, $z = 19$ and 20 Å, the maxima are at the center because the nearest W atoms are located in its vicinity for these heights. As expected, the electronic density images at $z = 20$ Å somewhat resemble the emitted current ones at large field, when the driving parameter is no more potential but density, but can be qualitatively different at low field (for instance, for 20V/nm and 1ML). In all cases, however, emission images (fig. 5) are less contrasted than density ones (fig. 6).

C. Energy distributions and densities of states

We show on fig. 7–9 the projected local density of states (PLDOS) $\rho^a_{jk}(\epsilon)$ provided by the DFT calculation for the 0ML–2ML configurations, as well as the state current densities (eq. 2). The total density of states is defined by: $\rho(\epsilon) = \sum_m \delta(\epsilon - \epsilon_m)$. $\delta(\epsilon - \epsilon_m)$ is the Dirac delta distribution centered on ϵ_m. PLDOS can be defined similarly by using real spherical harmonics $Y^a_{jk}(\mathbf{r})$ centered on atom a (=W or C): $\rho^a_{jk}(\epsilon) = \sum_m |\langle Y^a_{jk}|\Psi_m\rangle|^2 \, \delta(\epsilon - \epsilon_m)$ where jk are the usual angular momentum quantum numbers which define, for instance, the p_z, d_{z^2} and d_{xz} characters. Locality is obtained by enforcing the harmonics to be zero

outside spheres of radius r_a centered on atom a, r_a being the atomic radius, chosen here to be $r_a = 1.455\,\text{Å}$ for W and $0.863\,\text{Å}$ for C. The PLDOS can be approximated in different ways. For instance, using the step approximation for the delta functions on small intervals $[\epsilon, \Delta\epsilon_m] = [\epsilon_m - \Delta\epsilon_m/2, \epsilon_m + \Delta\epsilon_m/2]$: $\delta(\epsilon - \epsilon_m) = \frac{1}{\Delta\epsilon_m}$ when $\epsilon \in [\epsilon, \Delta\epsilon_m]$ and $\delta(\epsilon - \epsilon_m) = 0$ otherwise, we obtain:

$$\rho^a_{jk}(\epsilon) \approx \sum_{m/\epsilon\in[\epsilon,\Delta\epsilon_m]} \frac{|\langle Y^a_{jk}|\Psi_m\rangle|^2}{\Delta\epsilon_m} \tag{3}$$

The PLDOS gives qualitative information on where the electronic density in a given energy range is localized. We select on fig. 7–9 the spherical harmonics which point in the emission direction (z). The orbitals with significant weight on them are expected to contribute significantly to the emitted current density. Indeed, we showed in ref. 41 that there is a correlation between the current density associated to a state $|\Psi_m\rangle$ and the weights of its projections on the z-pointing harmonics.

The current density energy distribution $\frac{dJ}{d\epsilon}$ (CDED) can be defined similarly to the density of states from the state current densities J_m by: $\frac{dJ}{d\epsilon}(\epsilon) = \sum_m J_m\delta(\epsilon - \epsilon_m)$. Using the same approximation for the $\delta(\epsilon - \epsilon_m)$ distributions, we obtain the current density energy distribution $\frac{dJ}{d\epsilon}$ (CDED): $\frac{dJ}{d\epsilon}(\epsilon) \approx \sum_{m/\epsilon\in[\epsilon,\Delta\epsilon_m]} \frac{J_m}{\Delta\epsilon_m}$. Notice that the PLDOS and CDED form continuous spectra to which the discretized expressions given above are approximations. For instance, within the Fowler-Nordheim model, the CDED is a continuous function of energy given by eq. 8 in ref. 41.

The PLDOS presented here show that d tungsten orbitals have much stronger weights than p ones in the electronic density: in the energy band considered here, the p_z PLDOS is the smallest for the three 0ML–2ML configurations. The PLDOS have interesting features in common with the LDOS shown in ref. 43. Near the Fermi level, there is a minimum in the DOS for bulk tungsten which turns into a maximum for tungsten slabs in the LDOS associated to surface atoms (fig. 4 in ref. 43). A similar maximum is also clearly visible on the PLDOS of fig. 7 (top frame) nearly 0.5 eV below the Fermi level. It is mainly supported by the d_{xz} and d_{yz} PLDOS, as expected since these contribute significantly to the interlayer W–W bonds. The emitting states for 0ML are also located in the energy band of this maximum, typically within 1 eV below Fermi level (2 bottom frames of fig. 7). States close in energy to the Fermi level are indeed expected to overcome more easily the tunneling barrier.

In presence of carbon adsorbates, the 0ML maximum near the Fermi level disappears, both in the LDOS (fig. 5 and 6 in ref. 43) and the PLDOS associated to tungsten (fig. 8 and 9 here). As a result, the state currents also decrease in the band 1 eV below Fermi level. A significant part of the electronic density is transferred from tungsten surface atoms to carbon. For 1ML (fig. 8), this transfer induces maxima in the PLDOS associated to p_z carbon near 1.2 and 3.4 eV below Fermi level. These maxima are correlated to significant state currents in the same energy ranges (2 bottom frames of fig. 8). In the 2ML case, the electron transfer produces significant carbon PLDOS over a broad energy band, from Fermi level down to -5 eV, and emission from the same wide energy band (2 bottom frames of fig. 9). As a result, the transfer of electrons from tungsten to carbon induces a change in emission sites (fig. 4), but the decrease of emission from tungsten is not fully compensated by an increase of emission from carbon.

IV. CONCLUSION

We have studied the effect of the presence of carbon adsorbates on field electron emission from a tungsten surface using a three dimensional quantum mechanical model based on periodic DFT code coupled to a perturbation theory wavepacket propagation program. Globally, the presence of carbon reduces emission, this result is consistent with estimates performed with FN-type models. Our study evidences the fact that the effect of carbon coverage on metal field emission depends on several factors including the relative values of carbon and metal work functions as well as the nature of the metal-carbon bonds. In many instances, the metal work function is higher than the carbon one and carbon deposits lead to work functions decrease and emission increase[63]. As tungsten is a low work function metal, we find here the opposite effect. Besides, comparison of our 1ML and 2ML results shows that this emission reduction strongly depends on the nature of the metal-carbon bond. The double layer carbon deposit creates a strong perpendicular electric dipole which inhibits emission much more than the single layer one. Electron density migrates from tungsten to carbon, and the resulting decrease of emission from tungsten sites is not compensated by emission from the carbon sites. In a recent paper[41], we studied the effect of corrugation on emission from clean tungsten. The present results were obtained for tungsten contaminated with flat carbon layers. Combining both results, the next step could be to consider contami-

nation from corrugated carbon deposits. This is indeed this configuration which is expected to be the one observed in the experiments which motivate the present work[15–17].

We have presented in the present paper results from our emission model for extremely high values of the electric field. It is well known that at such high values, thermal effects appear (ref. 57 and chapter 3 in ref. 64) which are not included in our model. Such thermal effects result from couplings between the emitted electrons and the atom lattice of the electrode which induce phonon excitations, phase transitions and metal atom ejections. The present DFT calculation has been performed at fixed nuclei and coupling it to lattice dynamics is a technically difficult task never achieved, to our knowledge, up to now. However, it may be interesting to perform experiments taking advantage of the difference in time scales between electron emission which is fast and lattice distortion which is slow. By recording the emitted electrons as a function of time, one may be able to see the transition between emission at early times, equivalent to the conditions of the present study, and the one at later times, when thermal effects become significant. Besides, we have considered in the present and previous papers field emission from 3D materials, clean or not[40], flat or not[41]. A possible extension of the present work could focus on emission from 2D materials which give unconventional emission characteristics with respect to the electric field which differ from the usual Fowler-Nordheim law[65–67]. Indeed, the DFT model could be readily adapted to such low dimensionality materials.

V. ACKNOWLEDGEMENTS

Maykel Márquez-Mijares acknowledges fundind from CNRS for an invited scientist position as well as financial support from IRSAMC and from the mobility support of the cooperation service and cultural action (SCAC) of the French Embassy in Cuba.

---

* Electronic address: mmarquez@instec.cu

† Electronic address: bruno.lepetit@irsamc.ups-tlse.fr

[1] A. Simonin, J. Achard, K. Achkasov, S. Bechu, C. Baudouin, O. Baulaigue, C. Blondel, J. Boeuf, D. Bresteau, G. Cartry, et al., Nucl. Fusion **55**, 123020 (2015).

[2] H. P. L. de Esch, A. Simonin, C. Grand, B. Lepetit, D. Lemoine, M. Márquez-Mijares, T. Minea, L. Caillault, B. Seznec, T. Jager, et al., AIP Proc. **1869**, 060003 (2017).

[3] R. H. Fowler and L. Nordheim, Proceedings of the Royal Society of London A: Mathematical, Physical and Engineering Sciences **119**, 173 (1928).

[4] E. L. Murphy and R. H. Good, Physical Review **102**, 1464 (1956).

[5] A. Simonin, H. d. Esch, L. Doceul, L. Christin, F. Faisse, and F. Villecroze, Fusion Engineering and Design **88**, 1 (2013).

[6] R. S. Hemsworth, A. Tanga, and V. Antoni, Review of Scientific Instruments **79**, 02C109 (2008).

[7] R. Hemsworth, H. Decamps, J. Graceffa, B. Schunke, M. Tanaka, M. Dremel, A. Tanga, H. P. L. de Esch, F. Geli, J. Milnes, et al., Nuclear Fusion **49**, 045006 (2009).

[8] R. V. Latham, *High Voltage Vacuum Insulation: Basic Concepts and Technological Practice* (Elsevier, New-York, 1995).

[9] D. Alpert, D. Lee, E. M. Lyman, and H. E. Tomaschke, Journal of Applied Physics **38**, 880 (1967).

[10] G. Beukema, Physica **61**, 259 (1972).

[11] R. N. Bloomer and B. M. Cox, Vacuum **18**, 379 (1968).

[12] B. Bonin, Vacuum **46**, 907 (1995).

[13] A. Zeitoun-Fakiris and B. Juttner, Journal of Physics D: Applied Physics **21**, 960 (1988).

[14] Y. Yamamoto and T. Miyokawa, Journal of Vacuum Science and Technology B (Microelectronics and Nanometer Structures) **16**, 2871 (1998).

[15] K. Almousa Almaksour, Ph.D. thesis (2014), URL `https://tel.archives-ouvertes.fr/tel-01014658`.

[16] K. Almaksour, M. J. Kirkpatrick, P. Dessante, E. Odic, A. Simonin, H. P. L. de Esch, B. Lepetit, D. Alamarguy, F. Bayle, and P. Teste, Phys. Rev. ST Accel. Beams **17**, 103502 (2014).

[17] M. Márquez-Mijares, B. Lepetit, D. Lemoine, K. Almaksour, M. J. Kirkpatrick, P. Dessante, E. Odic, D. Alamarguy, F. Bayle, P. Teste, et al., J. Vac. Sci. Technol. B **34**, 061208 (2016).

[18] L. W. Nordheim, Proc. R. Soc. London, Ser. A **121**, 626 (1928).

[19] R. Burgess, H. Kroemer, and J. Houston, Phys. Rev. **90**, 515 (1953).

[20] J. He, P. H. Cutler, and N. M. Miskovsky, App. Phys. Lett. **59**, 1644 (1991).

[21] A. Modinos, Solid-State Electronics **45**, 809 (2001).

[22] R. G. Forbes, App. Phys. Lett. **89**, 113122 (2006).

[23] R. G. Forbes, J. H. B. Deane, A. Fischer, and M. S. Mousa, Jordan Journal of Physics **8**, 125 (2015).

[24] Y. Li, Y. Sun, and J. Yeow, Nanotechnology **26**, 242001 (2015).

[25] Z. B. Li, Ultramicroscopy **159**, 162 (2015).

[26] J. Peng, Z. Li, C. He, G. Chen, W. Wang, S. Deng, N. Xu, X. Zheng, G. Chen, C. J. Edgcombe, et al., Journal of Applied Physics **104**, 014310 (2008).

[27] M. Khazaei, A. A. Farajian, and Y. Kawazoe, Phys. Rev. Lett. **95**, 177602 (2005).

[28] Y. Gohda, Y. Nakamura, K. Watanabe, and S. Watanabe, Phys. Rev. Lett. **85**, 1750 (2000).

[29] Y. Gohda and S. Watanabe, Phys. Rev. Lett. **87**, 177601 (2001).

[30] Y. Gohda and S. Watanabe, Surface Science **516**, 265 (2002).

[31] Y. Gohda, Y. Nakamura, K. Watanabe, and S. Watanabe, Materials Science and Engineering A **327**, 1 (2002).

[32] Y. Gohda and S. Watanabe, J. Phys.: Condens. Matter **16**, 4685 (2004).

[33] S. F. Huang, T. Leung, B. Li, and C. Chan, Phys. Rev. B **72**, 035449 (2005).

[34] A. Mayer, N. M. Miskovsky, P. H. Cutler, and P. Lambin, Phys. Rev. B **68**, 235401 (2003).

[35] Z. Li, N. Xu, and H. J. Kreuzer, Phys. Rev. B **85**, 115427 (2012).

[36] P. Yaghoobi, K. Walus, and A. Nojeh, Phys. Rev. B **80**, 115422 (2009).

[37] S. Han, M. H. Lee, and J. Ihm, Phys. Rev. B **65**, 085405 (2002).

[38] Y.-W. Son, S. Oh, J. Ihm, and S. Han, Nanotechnology **16**, 125 (2005).

[39] C. Choong-Ki Lee, B. Lee, and S. Ihm, J. Han, Nanotechnology **18**, 475706 (2007).

[40] B. Lepetit, J. Appl. Phys. **122**, 215105 (2017).

[41] B. Lepetit, J. App. Phys. **125**, 025107 (2019).

[42] B. Lepetit, D. Lemoine, and M. Márquez-Mijares, J. App. Phys. **120**, 085105 (2016).

[43] M. Márquez-Mijares, B. Lepetit, and D. Lemoine, Surface Science **645**, 56 (2016).

[44] G. Kresse and J. Hafner, Physical Review B **47**, 558 (1993).

[45] G. Kresse and J. Hafner, Physical Review B **49**, 14251 (1994).

[46] G. Kresse and J. Furthmüller, Computational Materials Science **6**, 15 (1996).

[47] G. Kresse and J. Furthmüller, Physical Review B **54**, 11169 (1996).

[48] P. E. Blöchl, Physical Review B **50**, 17953 (1994).

[49] G. Kresse and D. Joubert, Physical Review B **59**, 1758 (1999).

[50] J. P. Perdew, K. Burke, and M. Ernzerhof, Physical Review Letters **77**, 3865 (1996).

[51] J. P. Perdew, K. Burke, and M. Ernzerhof, Physical Review Letters **78**, 1396 (1997).

[52] M. Methfessel and A. Paxton, Physical Review B **40**, 3616 (1989).

[53] H. J. Monkhorst and J. D. Pack, Physical Review B **13**, 5188 (1976).

[54] W. S. Koh and L. K. Ang, Nanotechnology **19**, 235402 (2008).

[55] S. Sun and L. K. Ang, Physics of Plasmas **19**, 033107 (2012).

[56] G. N. Fursey, Applied Surface Science **215**, 113 (2003).

[57] G. N. Fursey, IEEE Xplore Digital Library, Proceedings of the Young Researchers in Vacuum Micro/Nano Electronics (VMNE-YR) conference (2016), URL `https://ieeexplore.ieee.org/document/7880404/`.

[58] A. Kyritsakis, M. Veske, K. Eimre, V. Zadin, and F. Djurabekova, J. Phys. D: Appl. Phys. **51**, 225203 (2018).

[59] A. Kyritsakis and F. Djurabekova, Computational Materials Science **128**, 15 (2017).

[60] C. J. Fall, N. Binggeli, and A. Baldereschi, Phys. Rev. B **58**, R7544 (1998).

[61] C. J. Fall, N. Binggeli, and A. Baldereschi, Phys. Rev. B **66**, 075405 (2002).

[62] C. J. Fall, N. Binggeli, and A. Baldereschi, Phys. Rev. Lett. **88**, 156802 (2002).

[63] P. A. Khomyakov, G. Giovannetti, P. C. Rusu, G. Brocks, J. van den Brink, and P. J. Kelly, Phys. Rev. B **79**, 195425 (2009).

[64] G. Fursey, *Field emission in vacuum microelectronics* (Kluwer Academic/Plenum Publishers, 2005).

[65] Y. S. Ang and L. K. Ang, Phys. Rev. Applied **6**, 034013 (2016).

[66] Y. Ang, S.-J. Liang, and L. Ang, MRS Bulletin **42**, 505 (2017).

[67] Y. S. Ang and L. K. Yang, H. Y. Ang, Phys. Rev. Lett. **121**, 056802 (2018).

TABLE I: Parameters of optimized W(100) surfaces with 0ML, 1ML and 2ML carbon. Surface formation and adsorption energies (per carbon atom) as well as work function are given. The carbon atom heights are with respect to the metal surface, defined as the last tungsten atomic plane. Relaxation induces changes with respect to the bulk in the interlayer distances Δ_{ii+1} as shown on fig. 1. The present results are compared to those of ref. 43. The Δ_{ii+1} obtained in the context of ref. 43 had remained unpublished.

coverage	E_{surf}(eV/Å^2)	E_{ads}(eV/atom)	z_C(Å)	Δ_{12} (%)	Δ_{23} (%)	Δ_{34} (%)	W_F(eV)
0ML	0.2510	-	-	-11.71	2.28	-1.01	4.12
0ML (ref. 43)	0.2492	-	-	-11.23	2.17	-0.82	4.10
1ML	-	8.83	0.37	11.13	-2.60	0.04	4.23
1ML (ref. 43)	-	8.77	0.36	10.88	-2.45	-0.01	4.20
2ML	-	5.57	0.41, 1.42	15.28	-4.93	0.23	6.24
2ML (ref. 43)	-	5.55	0.42, 1.39	15.48	-4.56	0.33	6.15

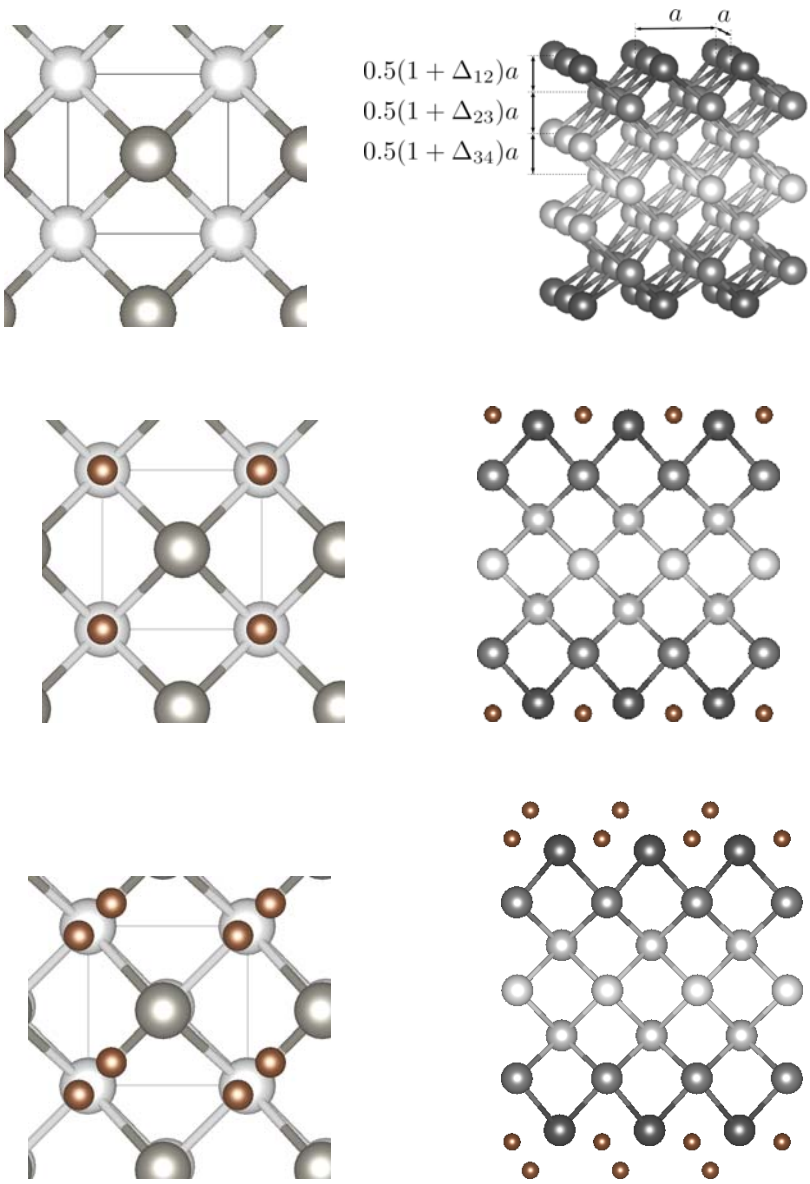

FIG. 1: The 100 tungsten surface with 0ML (top), 1ML (middle) and 2ML carbon atoms (bottom). Left: top view, right: side view. The carbon atoms are located on the hollow sites, as shown on table I. The thin lines (left) shows the unit cell used. The interlayer distance $\Delta_{i\,i+1}$ is defined on the top-right figure.

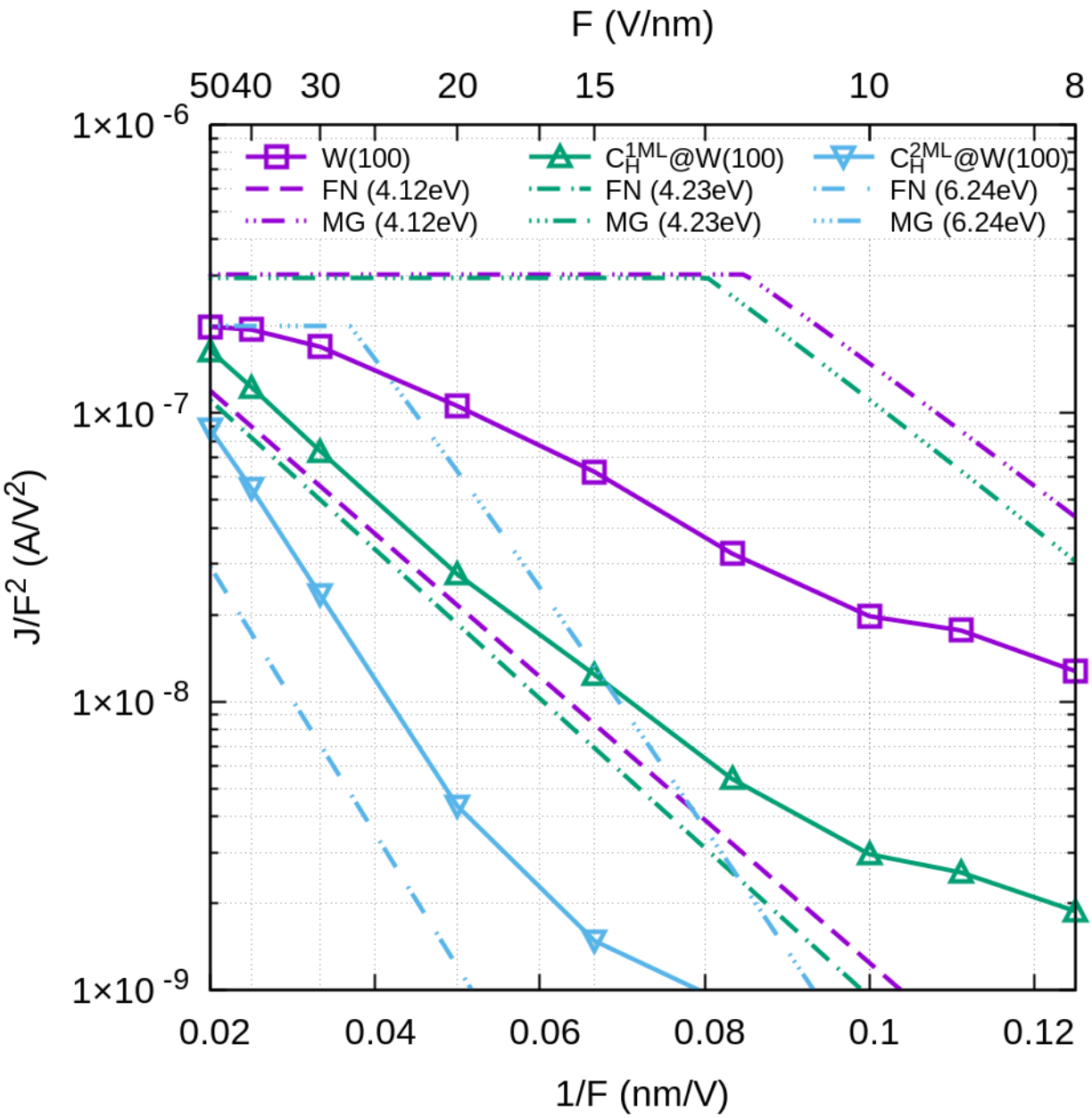

FIG. 2: Fowler-Nordheim plots of the averaged total emitted current density from our DFT model for 0ML (squares), 1ML (upward triangles) and 2ML (downward triangles). FN and MG analytical model results are also shown using the DFT work functions (also given on table I) for the same 3 configurations.

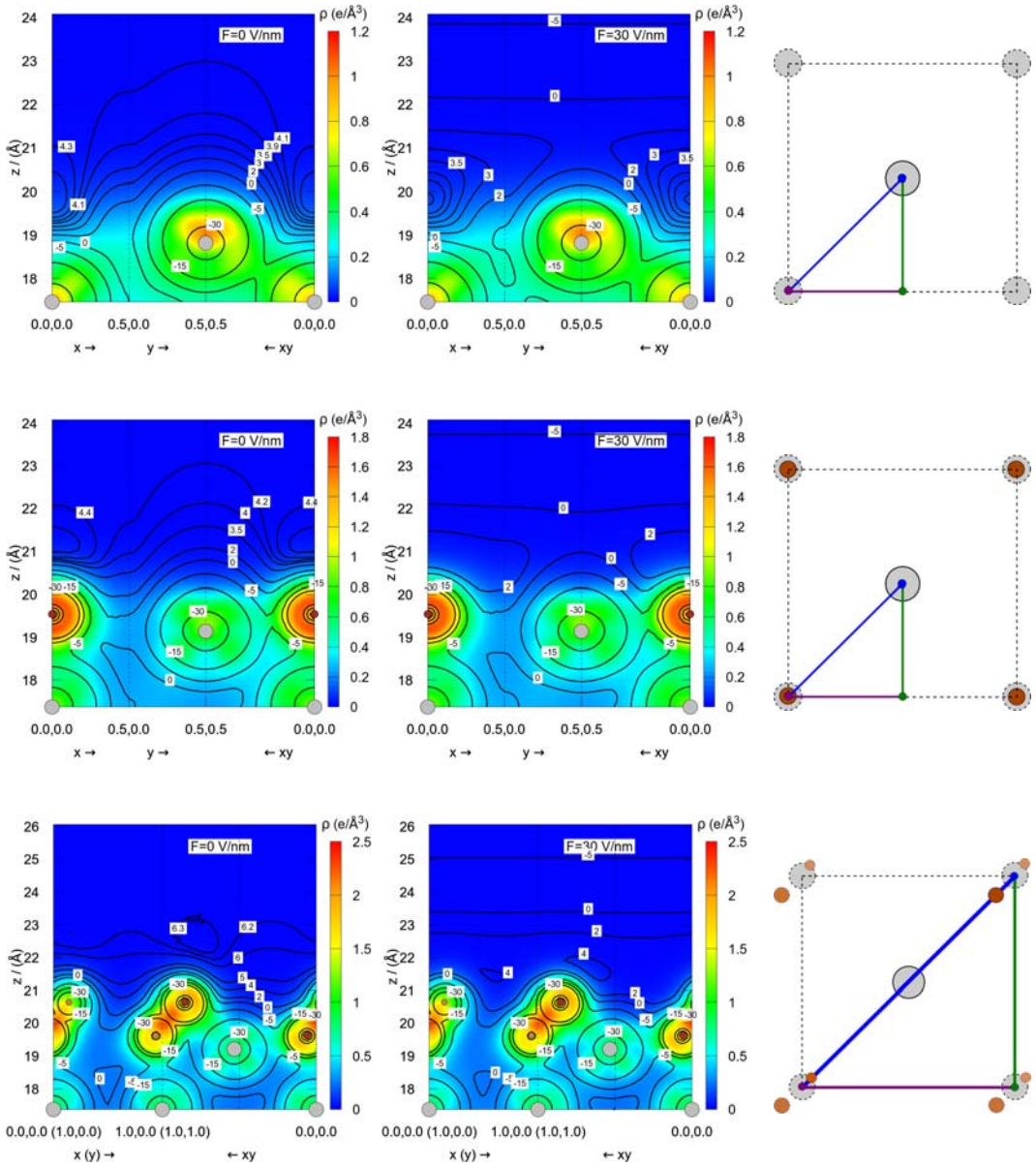

FIG. 3: Hartree potentials (contour lines, in eV) and electronic densities (color right scale in $e^-/\text{Å}^3$) on portions of planes which have in common the z axis which corresponds to the ordinate axis of the figure (in Å). The abcissa axis (in fractional coordinates) corresponds to the triangular pathes shown on the right hand side of the figure (color full lines): it can be x, y or the diagonal xy, as indicated by the symbols near the horizontal arrows below each frame (the notation $x(y)$ below the lowest frames indicate that the corresponding portion of the path is equivalently x or y). Grey and red disks correspond to W and C atom locations, respectively. The 0 energy is the Fermi level so that the potential is also the local work function. The potential contours are obtained for $F = 0$ (left) and $F = 30$ V/nm (right), for the 0ML, 1ML and 2ML configurations (from top to bottom). The electron density is the same for both left and right frames, it corresponds to $F = 0$.

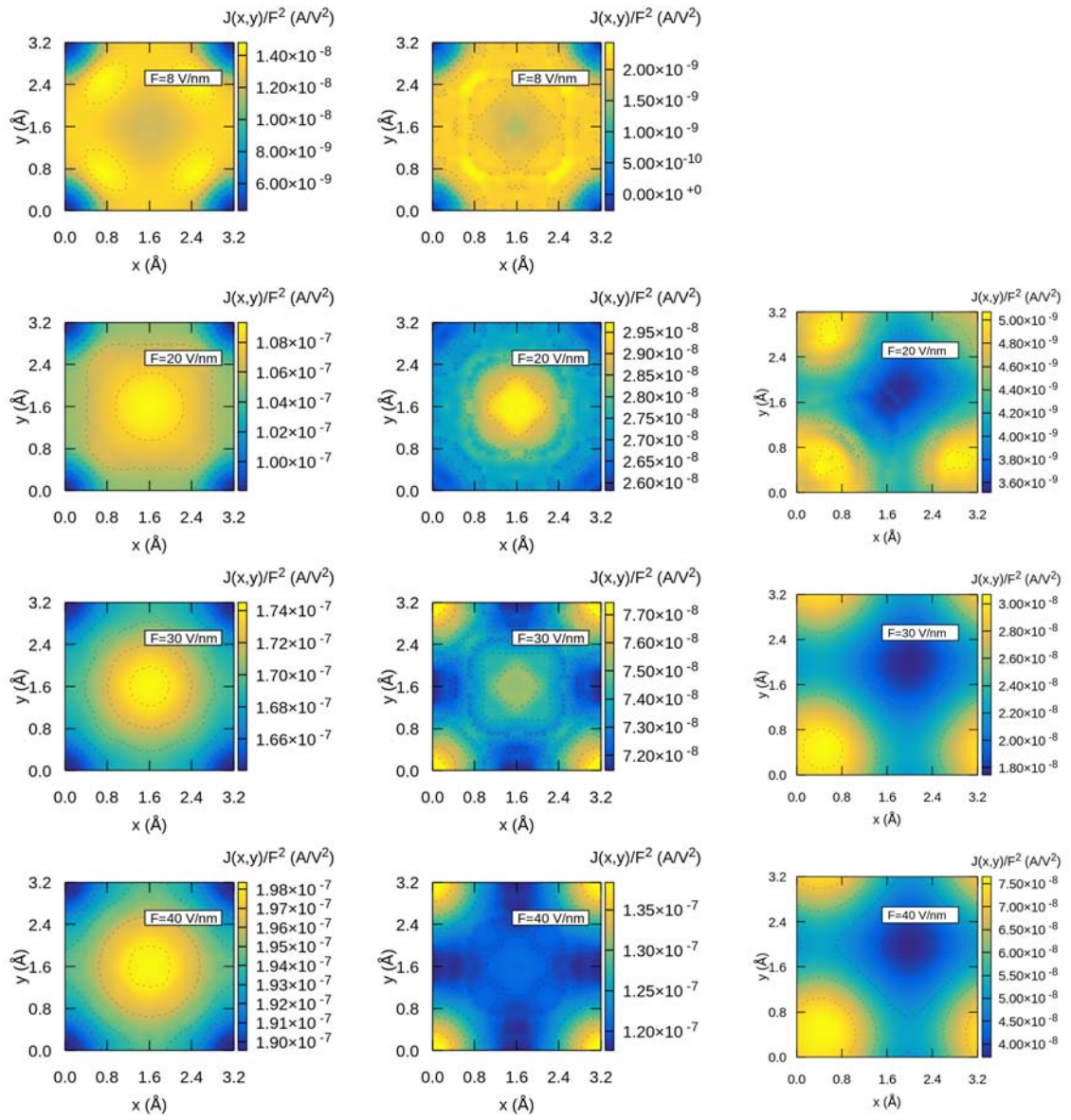

FIG. 4: Emission images, i. e. the local total current density $J(x, y)$ rescaled by F^2 to allow for a direct comparison with FN plots. From left to right: 0ML, 1ML and 2 ML. From top to bottom: F=8, 20, 30 and 40 V/nm.

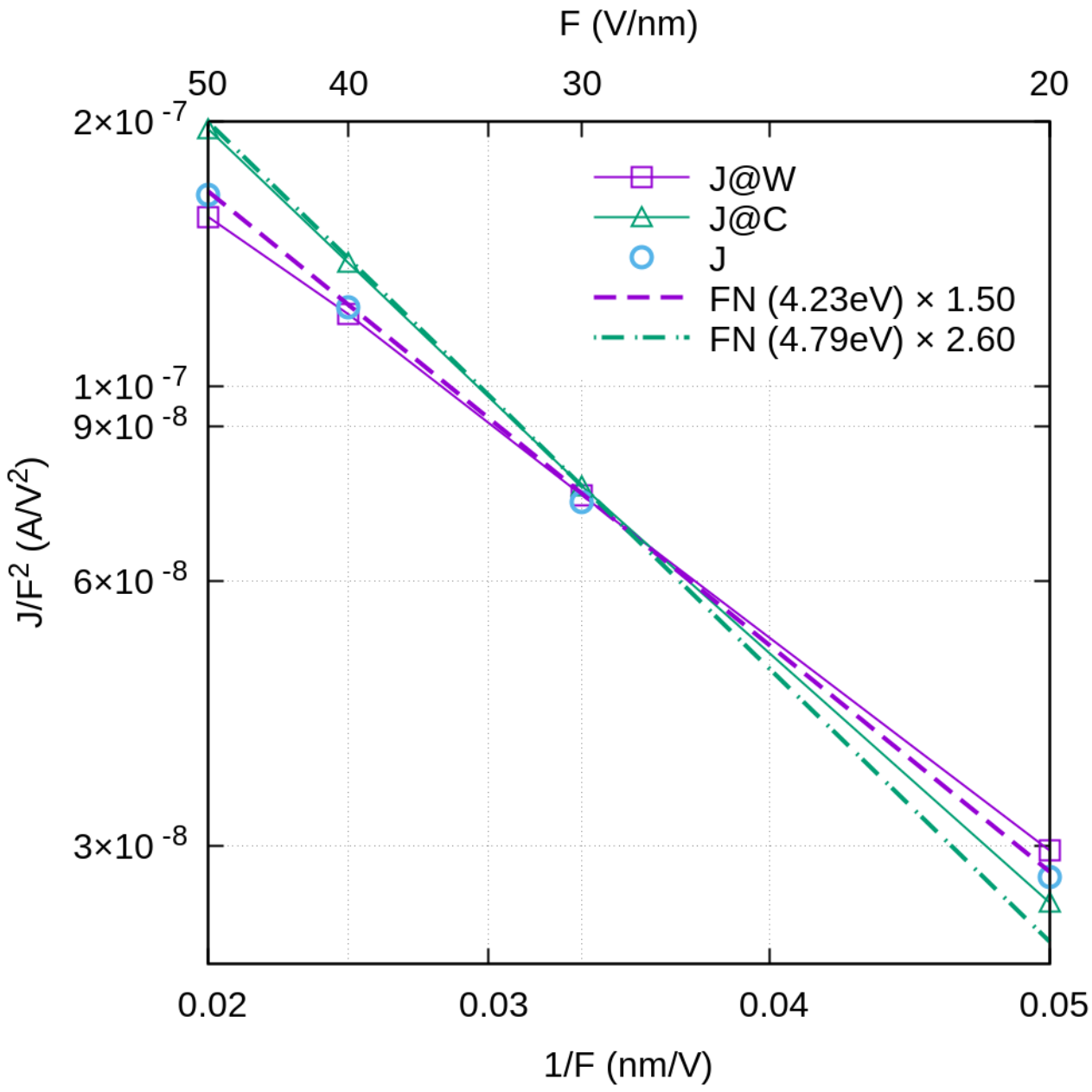

FIG. 5: Fowler-Nordheim plots for local and averaged current densities in the 1ML case. Squares: FN plot for the local current density $J(x = 0.5, y = 0.5)$ (W location), from DFT calculations. Triangles: FN plot for the local current density $J(x = 0, y = 0)$ (C location), from DFT calculations. Circles: FN plot for the averaged current density, from DFT calculations. Also shown are the FN plots for the Fowler-Nordheim models obtained with the work functions 4.23 eV (dashed line) and 4.79 eV (dashed-dotted line). These values are those of the local work functions for the W and C locations, respectively. The Fowler-Nordheim plots are rescaled by constant factors (1.5 and 2.6) which do not modify their slopes.

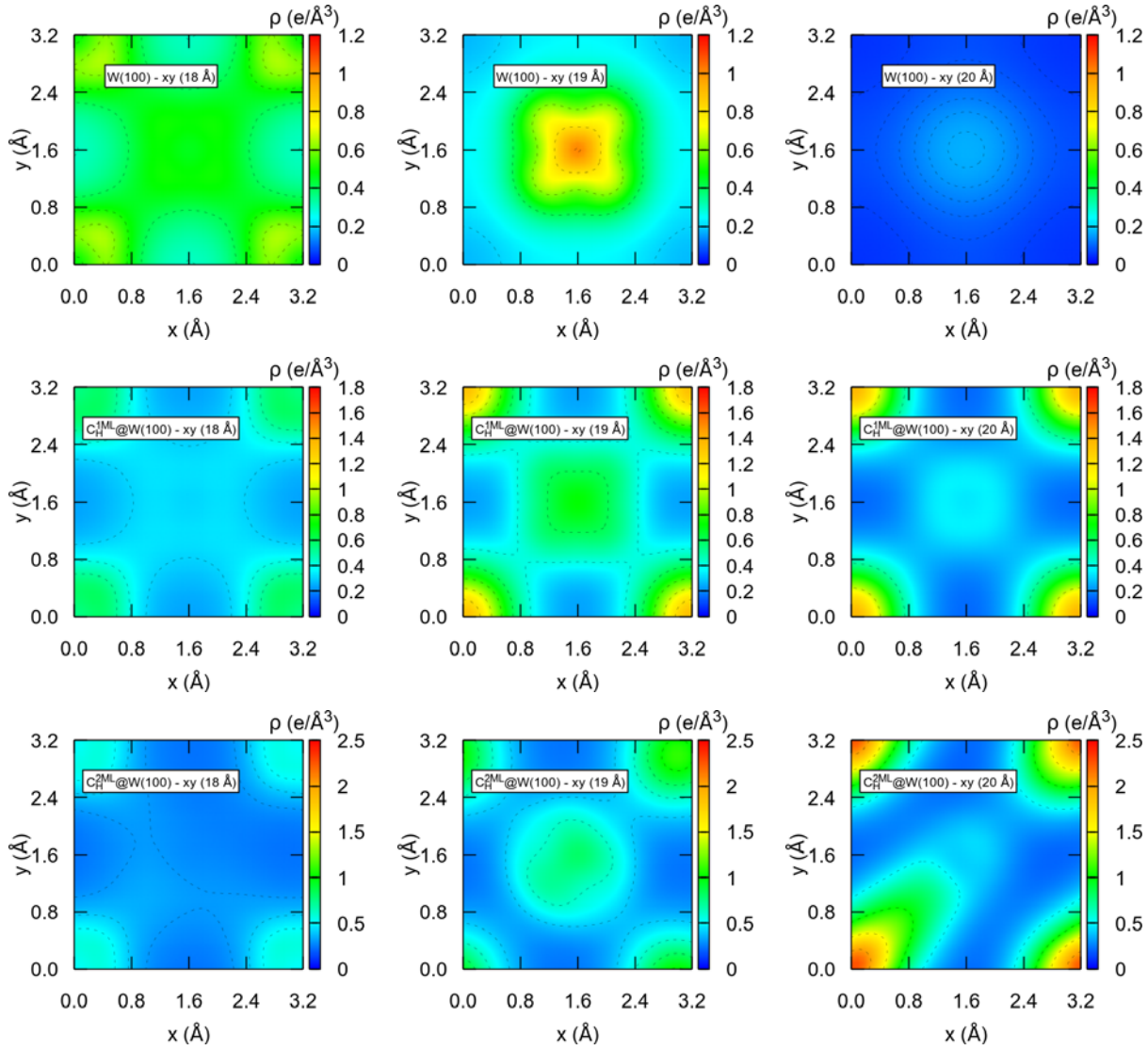

FIG. 6: Electronic density on the planes: $z = 18$, 19, 20 Å, from left to right. Top: 0ML, middle: 1ML; bottom: 2ML.

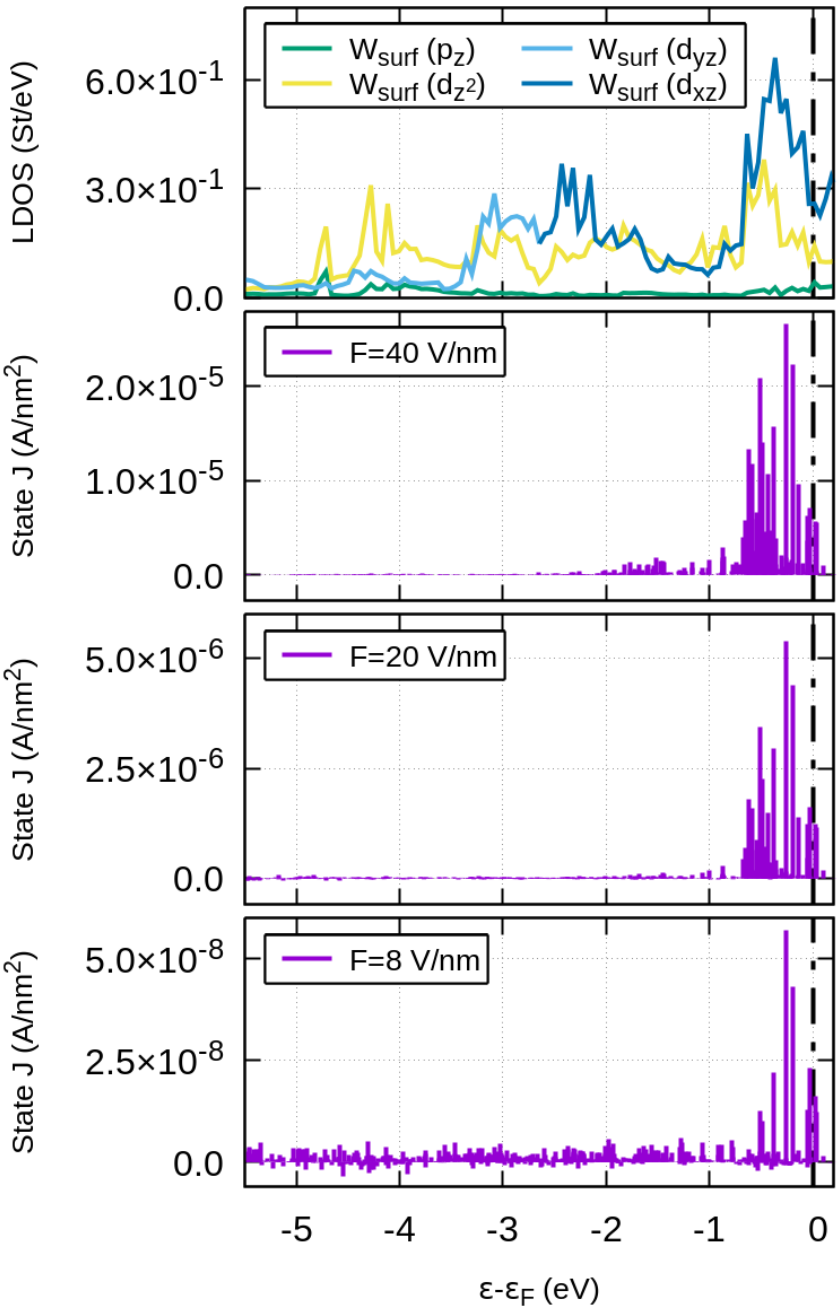

FIG. 7: Top: Projected local density of states (PLDOS, eq. 3) for spherical harmonics with z components (p_z, d_{z^2}, d_{xz}, d_{yz}), centered on the topmost tungsten atom and truncated to be confined inside a sphere of radius 1.455 Å. Results for d_{xz} and d_{yz} are degenerate. Bottom: state current density J_m as a function of the energy of the state m. Three field values (8, 20 and 40 V/nm) are considered. All data on this figure correspond to the 0ML configuration. The energies are relative to the Fermi level.

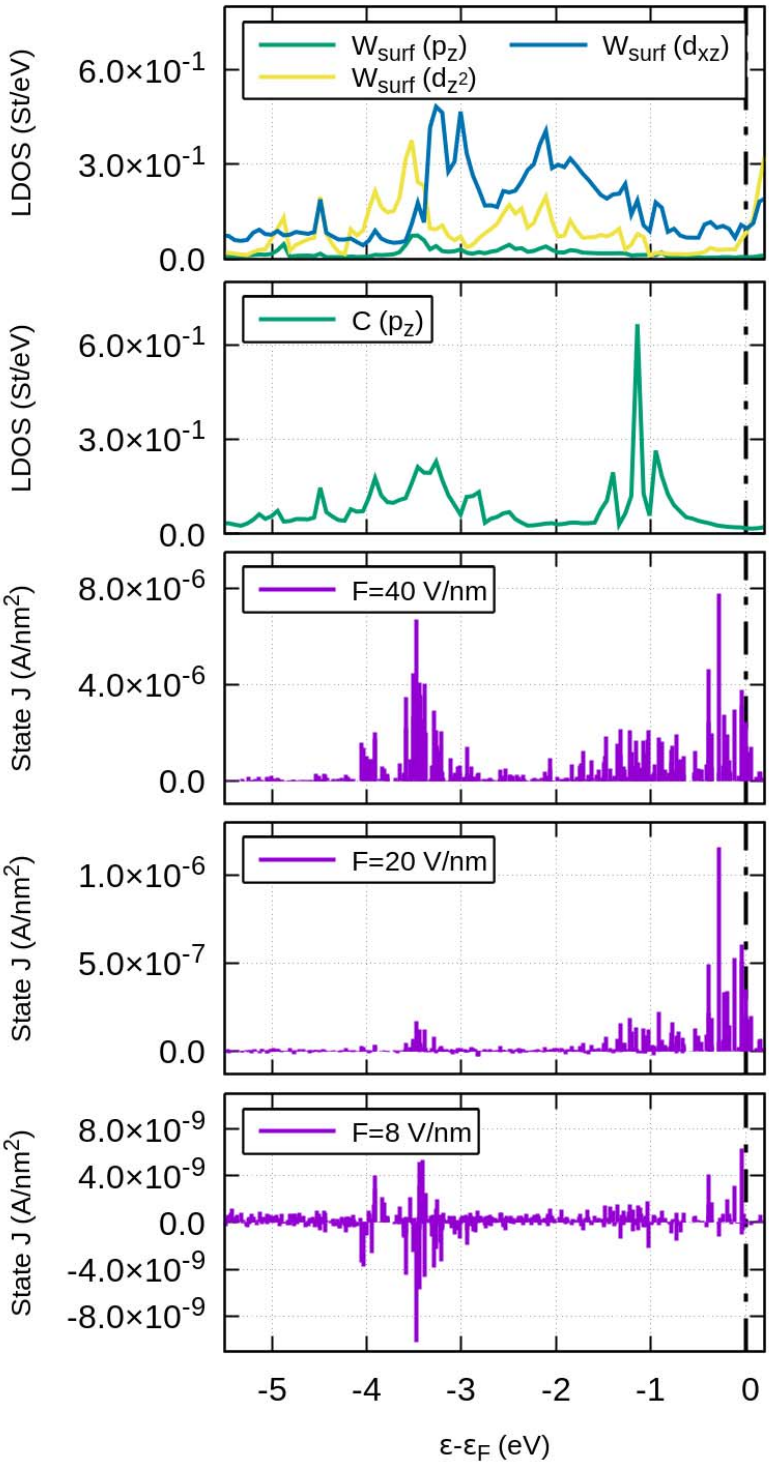

FIG. 8: Same as fig. 7, but for the 1ML case. A frame has been added (second from the top) to show projected local density of states associated to the adsorbed C atom. The p_z harmonic centered on the C atom is confined inside the sphere of radius 0.863 Å.

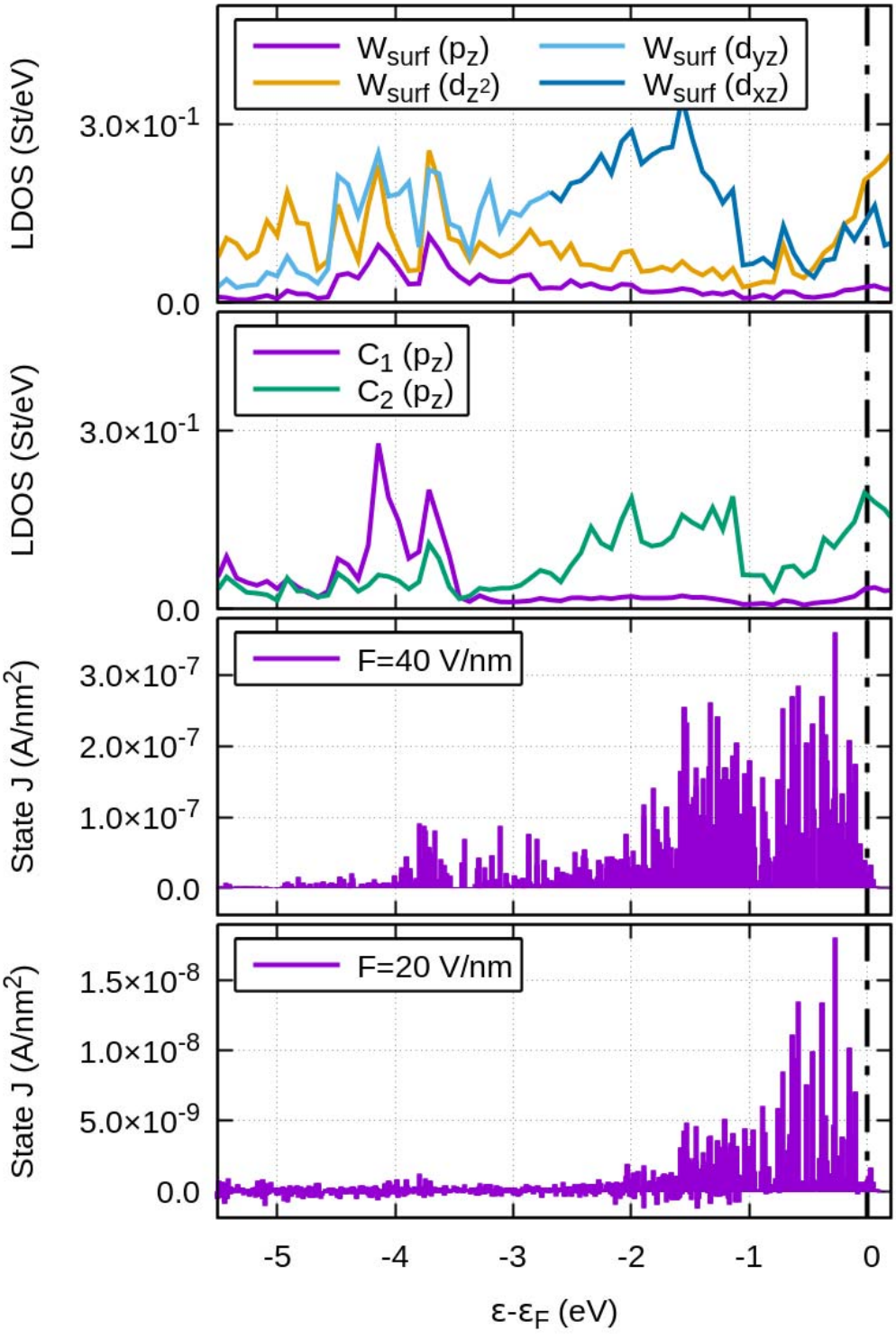

FIG. 9: Same as fig. 8 but for the 2ML case. Concerning the projected local density of states, C_1 and C_2 refer to the atoms with z_C =0.41 and 1.42 Å respectively (see table I and fig. 1).